NUMERICAL SOLUTION OF THE FLOW AROUND A TURBOFAN AND ITS WIND TUNNEL SIMULATOR

H.-Th. Bolms, D. Schwamborn

Deutsche Forschungsanstalt für Luft- und Raumfahrt

Göttingen, Germany

Abstract

In the process of aircraft development the main tasks of engine integration have changed with the progress of aircrafts and engines. The interference effects of turbofan engines increase with increasing bypass ratio. Therefore detailed investigations are required in order to avoid greater drag coefficients consuming the advantages of the new engines. Today's best experimental tools for these interference investigations are 'Turbine Powered Simulators' (TPS). Unfortunately, these simulators are not able to simulate the whole spectrum of characteristic features of a full scale engine correctly and simultaneously. Usually, these differences are deemed negligible.
In this investigation results of a numerical comparison between a modern turbofan under real conditions and one TPS of Deutsche Aerospace Airbus GmbH, Bremen (DA) are presented. The turbulent, axisymmetric three-dimensional engine flow is simulated numerically by using a finite-volume Navier-Stokes code. The influence of the Reynolds number on the aerodynamic quantities is demonstrated both for the actual engine and its scaled down version. The comparison of the scaled down actual engine and the simulator shows differences of the jet characteristics and the drag coefficients.
The results present an insight into the possibilities and restrictions of experimental engine simulations.

Introduction

New powerplant concepts for civil aviation aircrafts must meet the increased demands of the leading airline companies. Therefore the engine development objectives tend to larger specific power, longer lifecycles, less noise emissions and a more economical fuel consumption. These goals can be achieved effectively by increasing the propulsion efficiency and therefore by increasing the bypass ratio[1,2].
Today engines with a bypass ratio of about 6 are in service. The latest developments like the ADP (Advanced Ducted Propfan) of Pratt & Whitney will have bypass ratios of about 10-15. These engines are developments of the existing turbofan technology. Because of the greater fan diameter - compared with conventional turbofans with the same thrust - the integration of these engines is an important and difficult task.
The interferences between the engine, its suspension and the nacelle have an important influence on the flight characteristic. The interference drag of the engine and the nacelle of a conventional turbofan is in an order of about 5-10% of the total drag. Only if the high fuel saving potential of the future engines are not consumed by a higher interference drag the improvements of the advanced engines can really be exhausted. Therefore the exact prediction of the interferences becomes a main problem.
The numerical treatment of the complex and interactive flow between engine, pylon, wing and fuselage is extremely difficult and requires high qualifications of the computer codes used. Today it is possible to calculate these flow fields with Euler codes to obtain first trends[3].
Due to this situation the windtunnel experiment using engine simulators gains an increasing importance for both airplane and engine development. Great demands are made on these experiments. If the drag of the whole airplane is in the order of about 300 drag counts the drag share of the engines is in the order of about 10-15 drag counts. The aim of these experiments is not only the determination of the engine induced drag but also the determination of the differences between different configurations, i.e. drag in the order of about 1-3 drag counts must be determined exactly.
Today's best tool in engine simulation for air-breathing engines is the 'Turbine Powered Simulator' (TPS)[4]. The fan of a TPS is driven by a high pressure air turbine. The driving air expands in the turbine and simulates the primary jet of the actual engine. Unfortunately, despite its high technology standard such a simulator comprises some limitations for the simulation quality. These limits arise as a result of the scaling down process from the actual engine to the simulator and are of pure technical

and energetical nature only. The bypass ratio, the thrust partition, temperature and velocity ratios of primary and secondary jet and the simulation of the massflows are quantities with a direct influence on the simulation quality[5].

In this investigation the differences between an turbofan engine and its windtunnel simulator under realistic conditions and with correct boundary conditions are shown. The flows of the idealized (axisymmetrical) engines are calculated with a blockstructured 3D Navier-Stokes code[6] adapted for these calculations. It is necessary to use a Navier-Stokes code because the complex flow of an engine is characterised by several interactive phenomena like the plume and the entrainment effect, boundary and shear layers. Euler codes are not able to produce a realistic picture of these viscous and highly turbulent flows.

All calculations are performed at the Mach number M=0.17, corresponding to an operating point of the take-off phase. This operating point was selected because of the higher drag of the airplane and higher interference effects of the engine and the wing with extended flaps during this phase compared with cruising conditions. Many investigations of the take-off phase are performed in wind tunnel experiments with engine simulation. Therefore it is necessary to simulate the engine for this phase correctly, in order to determine the interference drag.

Navier-Sokes Solver

Governing Equations

The time dependent Navier-Stokes equations can be written in integral form using a cartesian frame of reference as

$$\frac{\partial}{\partial t}\int\int\int_{Vol}\overline{U}\;dVol+\iint_{S}\overline{H}\bullet\overline{n}\;dS \qquad (1)$$

where $\overline{U}$ is the solution vector of the volume-averaged mass, momentum and the total energy

$$\overline{U} = (\rho, \rho u, \rho v, \rho w, \rho E)^T \qquad (2)$$

with u, v, w being the components of the velocity, the density ρ and the total energy E

$$E = e+\frac{1}{2}(u^2+v^2+w^2) \qquad (3)$$

with the mass averaged internal energy

$$e = \frac{p}{\rho(\kappa-1)} \qquad (4)$$

where p is the pressure and κ denotes the ratio of the specific heats. The unit normal vector of the surface S of the volume Vol is denoted by $\overline{n}$; $\overline{H}$ is the flux tensor.

The turbulent flows in this investigation were calculated with the algebraic turbulence modell of *Baldwin & Lomax*[7] with modifications according to *Granville*[8] considering the pressure gradients, since the $k-\omega$ two equation turbulence model according to *Wilcox*[9] is still in preparation up to now.

Solution Scheme

For the discretization of the full Navier-Stokes equations the finite-volume scheme is used, which has been developed by *Jameson et al.*[10] for the Euler equations. Here the physical domain is divided in hexahedral cells. The discrete values of the flow quantities are located in the center of the cell. The discretization in space and time is done seperately. The fluxes across the cell faces are averaged from neighbouring cells which is equivalent to central differencing. Artificial diffusion terms are used to stabilize the solution. These damping terms are the blend of second and fourth order differences[10]. After the discretization of the Navier-Stokes equations with respect to space the integration in time is performed with a linearized four-stage Runge-Kutta scheme. Since we are only interested in steady state solutions, the method of local time steps is applied to accelerate the convergence.

Boundary Conditions

In order to describe the problem under consideration it is necessary to match the boundary conditions. Besides the 'classic' boundary conditions for the description of walls, wakes and the far field we newly implemented some conditions for the description of axisymmetrical engine flows allowing realistic calculations with parameters provided by the engine manufacturers.

At fan inflow faces the flow quantities are calculated as functions of the static pressure. At engine outflow faces like the fan- or turbine-exit area the momentum ρu, the temperature T, the spin β and the radial velocity component w are fixed as functions of the radius, according to the theory of characteristics. The boundary condition for centerlines allows the treatment of non hexahedral cells occuring at the centerline combined with a special handling of the border cells. The periodic boundary condition saves a lot of CPU-time and memory. It is possible to take rotating walls like the spinner into consideration.

Due to the complex geometry and the algebraic turbulence model it is necessary to divide the physical domain into several blocks. At the time the code was developed one reason for the block structure was the lack of sufficient CPU-memory. Today we use an in-core version when we perform calculations on a NEC-SX3 avoiding the time consuming I/O of the block management.

Grid Generation

In this investigation body-fitted, block structured meshes are used. Using an interactive grid generation tool of *Ronzheimer et al.*[11] an H-type grid structure in streamwise direction is generated. Since the consistency of cell-centered schemes is sensitive to irregularities and discontinuities[12] the generation of the grids is established by the solution of an elliptic system of equations. In regions where great flow gradients are expected the density of grid nodes is increased distinctly. Since axisymmetrical flow is calculated, only two grid planes in circumferential direction are required. Therefore the threedimensional grid is generated by rotating the twodimensional grid about the centerline by two degrees.

Verification

The new implemented boundary conditions are verified with experimental data presented by *Mason et al.*[13] for nozzle flows. The numerical calculations are performed for a free-stream Mach number of M=0.4 and two nozzle pressure ratios of p_{tj}/p_∞=2.0 and p_{tj}/p_∞=2.9. One result of the verification is shown in this investigation. At seven planes behind the nozzle exit area pitot pressure ratios have been measured with a probe. The location of these planes is shown in **figure 1**, D denotes the diameter of the nozzle exit. In **figure 2** the pitot pressure ratios $p_{tj}/p_{t\infty}$ are plotted versus the dimensionless radius at the above mentioned planes for the nozzle pressure ratio of p_{tj}/p_∞=2.0. The symbols represent the experimental data, the lines show results of the Navier-Stokes calculation.

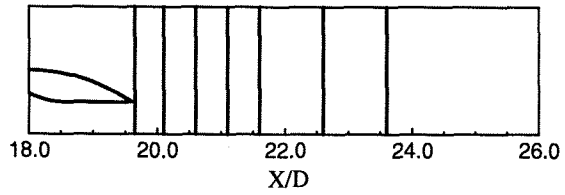

Fig. 1: Measurement planes behind the nozzle

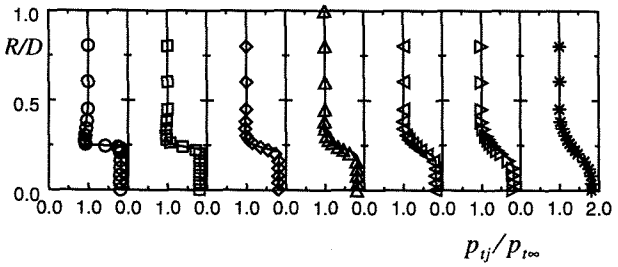

Fig. 2: Pitot pressure ratios behind the nozzle

The numerical results correspond verry well with the experimental data. Therefore it is possible to calculate a realistic picture of the jet mixing process.

Actual Engine

Figure 3 shows the full scale engine used in this investigation. It is a modern turbofan engine producing a thrust of about 25000 lb. It meets the power requirements for the A320. It is a high bypass turbofan engine with a bypass ratio of about 5.5 and a fan pressure ratio of about 1.6. It has a full length nacelle with a common nozzle.

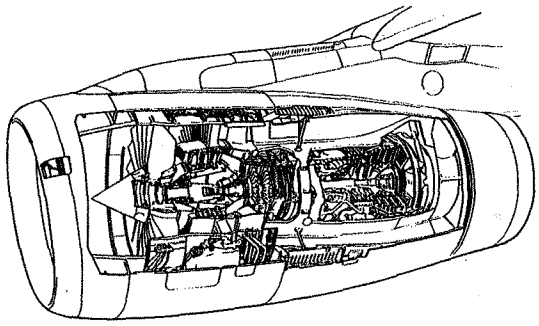

Fig. 3: Full scale engine

For the numerical calculation only the 12 o'clock section of the engine is used. In order to determine the Reynolds number effect of the calculation two calculations were performed: the full scale engine and a scaled engine. The scale of MM=1/13.6 is the same like the scale of the TPS. The scaled down engine is also used for comparison with the TPS results. Therefore no Reynolds number effects will occure within the comparison.

Results

Grid Generation. The grid used for the calculation of the turbofan consists of 12 computational blocks and of about 47000 grid points in total. A detail view of the block structure around the engine is shown in **figure 4**. The far field in front and normal to the engine is about 3 nacelle cords away and behind the engine about 10 nacelle cords away. In streamwise direction 168 grid points are distributed on the nacelle surface. The nozzle exit area is represented by 70 grid points in radial direction. In contrast to the actual engine the trailing edges of the nacelle and the core cowl are not blunt. Further no struts or other installations like thrust reversers are taken into consideration.

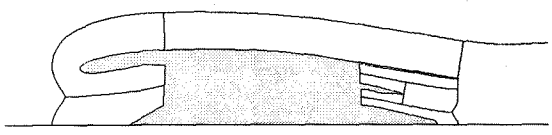

Fig. 4: Block structure of the full scale engine (detail)

The averaged mean thermodynamic parameters used for the calculations are listed in **table 1** both for the full scale engine and the scaled engine and are compared with the results of the calculations. The differences between the provided and the calculated data are due to the inviscid calculations used for the determination of the exit planes conditions of the fan and the turbine.

	provided	*calculated*	
	full scale	full scale	scale MM=1/13.6
fan pressure ratio π_F	1.6	1.6	1.6
nozzle pressure ratio $\bar{p}_{t\ nozzle}/p_\infty$	1.55	1.55	1.5488
nozzle temperature $\bar{T}_t$ [K]	414	411.77	411.38
jet velocity $\bar{u}_{nozzle}$ [m/s]	307	304.99	306.84
fan mass flow $\dot{m}_{Fan}$ [kg/s]	362	360.27	1.641
bypass ratio μ	5.3	5.3	5.3
netto thrust F [kN]	90	89.1	0.485

Tab. 1: Comparison of actual engine parameters with calculated ones

	full scale	scale *MM*=1/13.6
c_{Dp}	-0.857637	-1.03486
$c_{D\tau}$	3.3243E-03	3.86889E-02
c_D	-0.8854313	-0.996173

Tab. 2: Drag coefficients

Pressure and Drag Distribution. The pressure distributions on the actual engine nacelle surface (full scale - dashed line and scaled - solid line) are shown in **figure** 5. The pressure coefficient c_p is used:

$$c_p = \frac{p - p_\infty}{\rho/2\ u_\infty^2} \tag{5}$$

The differences in pressure distribution on the outer nacelle surface are negligible. The stagnation point on the nacelle is located for both Reynolds numbers at 1.4% of the cord length on the outer surface. The acceleration of the air around the full scale nacelle leading edge is larger than the acceleration at the scaled nacelle. In both cases separation occures at the inlet contour.

For a better comparison the drag coefficient c_D is calculated as

$$c_D = c_{Dp} + c_{D\tau} \tag{6}$$

with the drag coefficient c_{Dp} depending on the static pressure

$$c_{Dp} = \frac{1}{\rho/2\ u_\infty^2 \pi r_m^2} \sum^{i} (p_\infty - p_i)\, A_{i\perp} \tag{7}$$

and the drag coefficient $c_{D\tau}$ depending on the skin friction:

$$c_{D\tau} = \frac{1}{\rho/2\ u_\infty^2 \pi r_m^2} \sum^{i} \tau_{Wi}\ A_{i\parallel} \tag{8}$$

The skin friction coefficient c_f

$$c_f = \frac{\tau_W}{\rho/2\ u_\infty^2} \tag{9}$$

is shown in **figure 6** for the full scale nacelle and in **figure** 7 for the scaled nacelle. Both distributions are similar, the quantitative differences are due to the influence of the Reynolds number onto the skin friction. Both configurations show a small secondary separation at about x/L=0.1 for the full scale engine and at about x/L=0.09 for the scaled engine.

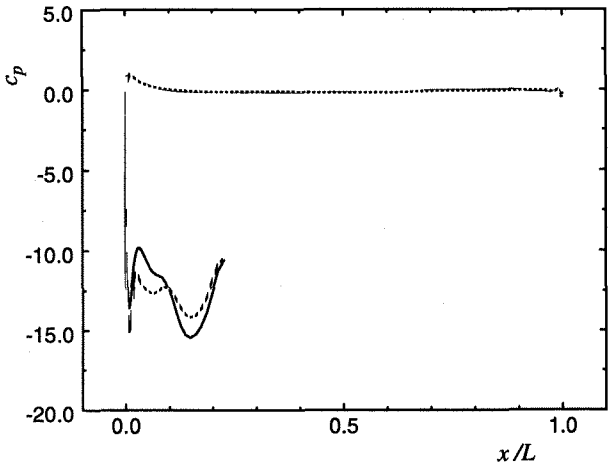

Fig. 5: Nacelle surface pressure distributions

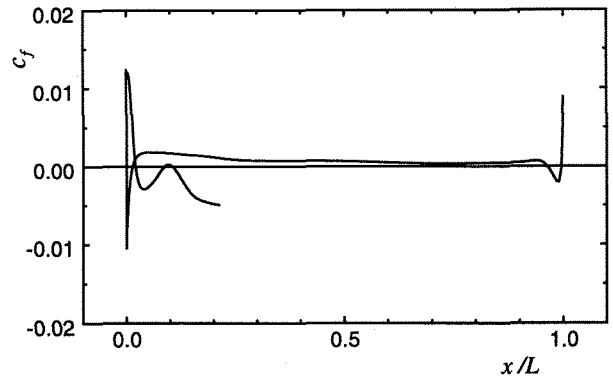

Fig. 6: Skin friction distribution for the full scale nacelle

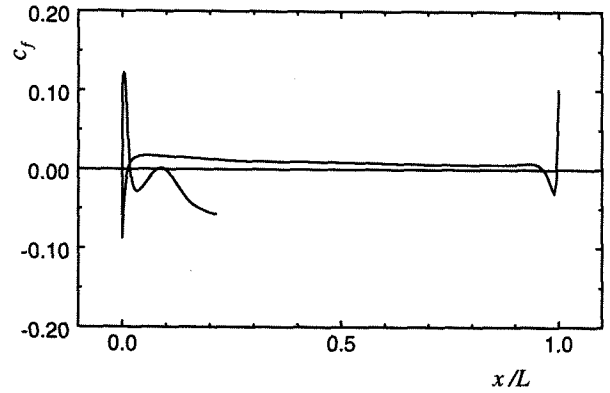

Fig. 7: Skin friction distribution for the scaled nacelle

The differences between the drag coefficient c_D of the full scale and the scaled nacelle are due to the large differences of the inlet flow. **Table 2** shows the calculated drag coefficients both for the full scale and the scaled engine.

To investigate the effect of the engine and its jet on the flow field around the engine we look at the pressure distribution at three planes above the engine (z/L=0.3, 0.4, 0.5). The three planes and the engine are shown in **figure 8**. The considered region includes the standard location of the wing. In **figure 9** the pressure distributions are shown for the scaled engine. The influence of the engine and its jet decreases with increasing distance. At x/L=0 the influence of the stagnation point is dominant. Between $x/L \cong 0.5$ and $x/L \cong 1.5$ a significant pressure rise occures. The air is decelerated for about one engine length beginning at the rear nacelle.

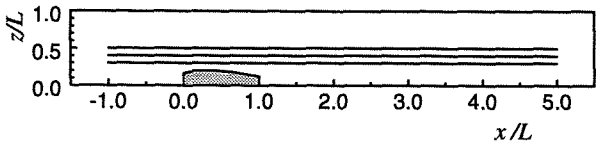

Fig. 8: c_p-planes above the engine

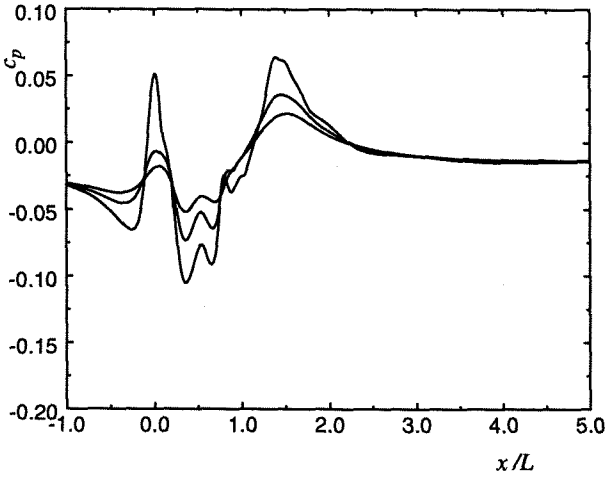

Fig. 9: Pressure distributions above the scaled engine

Inlet Flow. In **figure 10** the inlet Mach number distribution is shown for the scaled engine. The difference between two isolines is ΔM=0.05. The air is accelerated around the leading edge of the nacelle starting at the stagnation point located at the outer surface . At 2.1% of the cord length the flow separates. The bold line represents u=0 *m/s*. Due to the separation a large area occures where the Mach number is higher than 0.7.

Jet Characteristics. The jet characteristics of the full scale and the scaled engine are very similar, the differences are negligible. Therefore the jet characteristics are shown for the scaled engine only. In **figure 11** the ratios of the

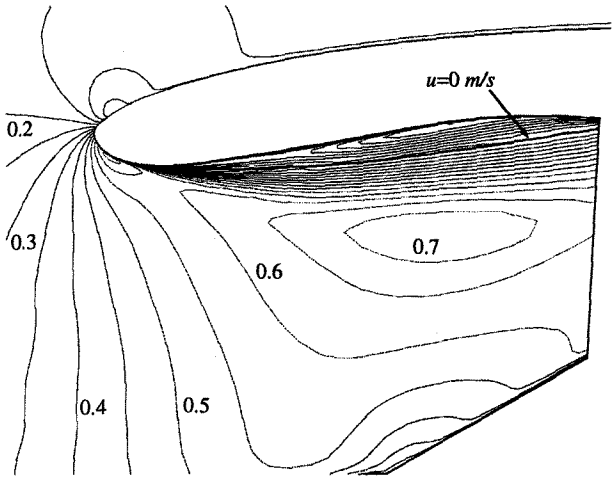

Fig. 10: Mach number isolines scaled engine inlet

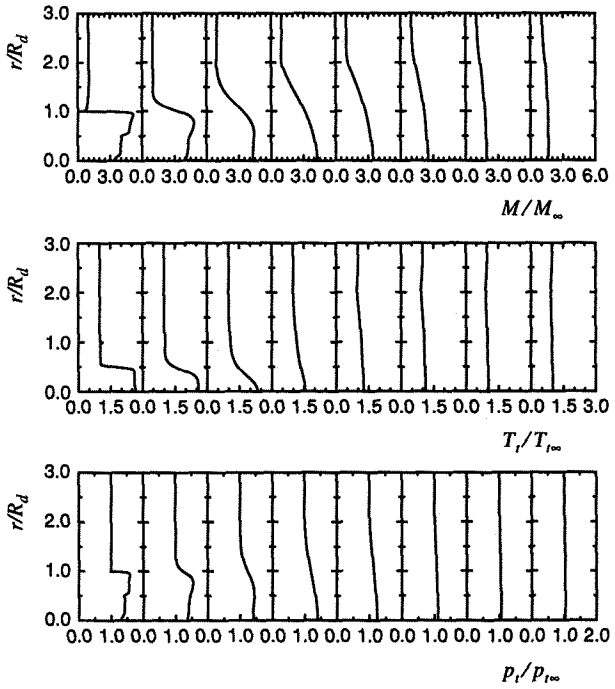

Fig. 11: Mach number, temperature and stagnation pressure profiles of the scaled engine jet

Fig. 12: Mach number isolines of the scaled engine

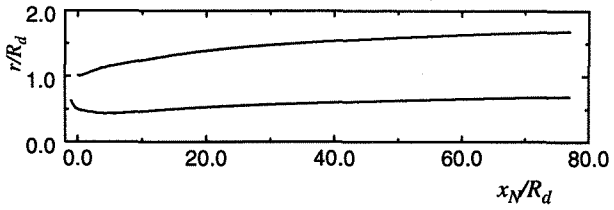

Fig. 13: Streamlines behind the scaled engine

Mach number, the temperature and the stagnation pressure of the jets to the free-stream values are plotted as functions of the dimensionless radius at eight planes behind the fan nozzle exit: x_N/R_d=0, 1, 2.5, 5, 10, 20, 35 and 50. The Mach number isolines around the engine are shown in **figure 12** (ΔM=0.05). In **figure 13** streamlines starting at the trailing edges of the core cowl and the nacelle are shown. Note, however, that the radial coordinate is scaled up ten times for better visualization. The primary and secondary jet show the expected characteristics. The wakes of the nacelle, the core cowl and the plug disappear quickly. The hot jet of the turbine flow is mixed with the cold fan flow within about one nacelle length. At x_N/R_d=50 the stagnation pressure ratio distribution is nearly even, the jet disperses.

TPS

For the simulation of the actual engine a TPS *TDI1500* of *Tech Development Inc.* is used by DA. The simulator has been used for wind tunnel experiments at several Airbus models; the scale is *MM*=1/13.6. **Figure 14** shows the TPS without the nacelle and the cowlings. The nacelle is similar to the actual one, i.e. the leading edge shape is the same like the actual one, but the inlet is about 25% longer than the scaled actual one. The nozzle shape is modified, the diameter is about 3.4% greater than the scaled actual one. The spinner of the TPS has an elliptic shape in contrast to the actual conical one. The core nozzle is extended about 5 *mm* out of the fan nozzle. Therefore in contrast to the actual engine an unmixed version results from this modification. The mean quantities of the simulator are listed in **table 1** for the operation point under consideration (*M*=0.17).

fan pressure ratio π_F		1.605
fan nozzle pressure ratio $\bar{p}_{t\ Fnozzle}/p_\infty$		1.46
fan nozzle temperature $\bar{T}_{t\ F}$	[K]	332
fan jet velocity $\bar{u}_{Fnozzle}$	[m/s]	282.3
fan mass flow $\dot{m}_{Fan}$	[kg/s]	1.53
turbine nozzle pressure ratio $\bar{p}_{t\ Tnozzle}/p_\infty$		1.36
turbine nozzle temperature $\bar{T}_{t\ T}$	[K]	186
turbine jet velocity $\bar{u}_{Tnozzle}$	[m/s]	177.4
turbine mass flow $\dot{m}_T$	[kg/s]	0.71
mass flow ratio $\dot{m}_F/\dot{m}_T$		2.15

Tab. 3: Mean quantities of the simulator

Results

Grid Generation. The complete grid for the DA-TPS consists of 13 computational blocks and about 64500 grid points in total. A detailed view of the block structure around the TPS is shown in **figure 15**. The design of the far field boundary is the same for both the TPS and the actual engine. In streamwise direction 163 grid points are distributed over the nacelle surface. Both nozzle exit areas are represented by 77 grid points in radial direction in total. The trailing edges are blunt and no struts or rakes are taken into account.

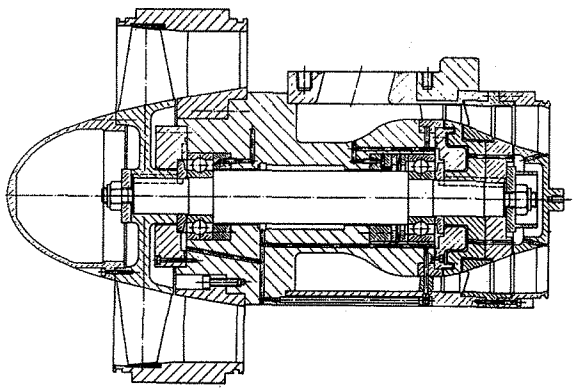

Fig. 14: Sectional view of the TPS TDI1500

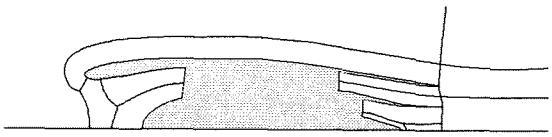

Fig. 15: Block structure of the DA-TPS (detail)

Pressure and Drag Distribution. The nacelle surface pressure distribution is compared with the scaled actual one in **figure 16** (TPS - solid line and scaled engine - dashed line). The stagnation point on the TPS nacelle is located at 0.9% of the cord length. The difference of the location is due to the different mass flows of the scaled actual engine and the TPS. The fan mass flow of the TPS is used only for the simulation of the secondary cycle. Therefore less air flows through the TPS inlet.
The pressure distributions on the outer nacelle surfaces of the TPS and the scaled engine show only small differences. The acceleration around the leading edge is in the same order for both engines. Due to the smaller mass flow of the TPS the flow separates at 6% of the cord length. Since the TPS inlet is longer than that of the scaled engine the separation reattaches in front of the fan at 25% of the cord length. These effects of the TPS inlet flow are also shown for the skin friction coefficient in **figure 17**.
The drag coefficients are listed in **table 4**.

c_{Dp}	$c_{D\tau}$	c_D
-0.615076	3.6233E-2	-0.578843

Tab. 4: Dag coefficients of the TPS

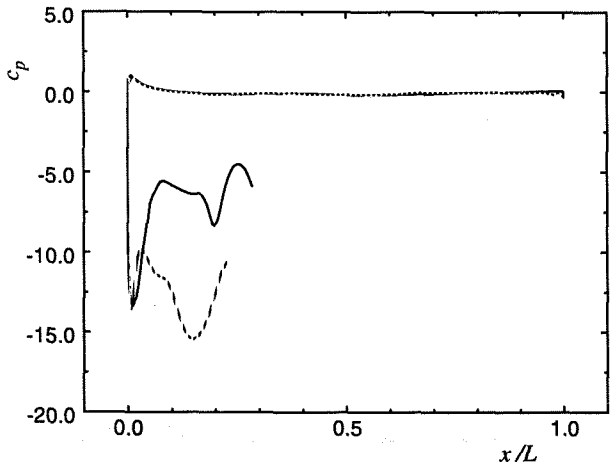

Fig. 16: Comparison of nacelle pressure distributions

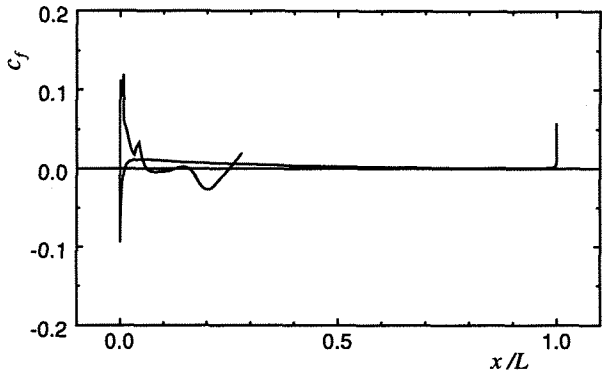

Fig. 17: Skin friction distribution TPS nacelle

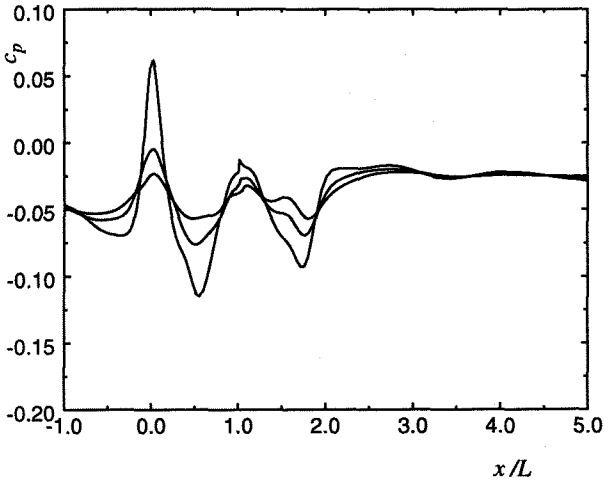

Fig. 18: Pressure distributions above the TPS

The effect of the TPS on the surrounding pressure distribution is shown in **figure 18**. The same planes are used (see also figure 8). The effect of the stagnation point of the TPS is of about the same order as for the scaled engine. A significant difference occures in the region after the nozzle. The flow of the TPS is accelerated in the region $1<x/L<1.75$. Such an effect doesn't exist for the scaled engine. After this acceleration a strong deceleration occures.

Inlet Flow. The inlet Mach number distribution of the TPS is shown in **figure 19**. Again the increment between two lines is $\Delta M=0.05$ and the bold line represents $u=0$ *m/s*. The accelerated air separates at 5% of the cord length. For the TPS the separation occures later compared with the scaled engine, since the mass flow is smaller and the contour of the nacelle doesn't change. The region of the secondary seperation is larger than for the scaled engine. It is located between 13% and 16% of the cord length (see also figure 17). The flow reattaches at 25% of the cord length. Since the mass flow is smaller a highest Mach number of about 0.5 occures in the TPS inlet.

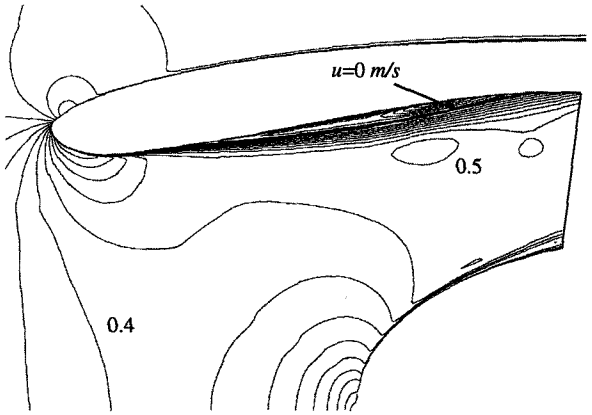

Fig. 19: Mach number isolines TPS inlet

Jet Characteristics. The Mach number distribution around the TPS is shown in **figure 20** (ΔM=0.05). In **figure 21** the ratios of the Mach number, the temperature and the stagnation pressure of the jets to the free-stream values are plotted as functions of the dimensionless radius at eight planes behind the fan nozzle exit: x_N/R_d=0, 1, 2.5, 5, 10, 20, 35 and 50. In **figure 22** streamlines starting at the trailing edges of the core cowl and the nacelle are shown. The radial coordinate is again scaled up ten times for better visualization.

The TPS jet can be divided in axial direction into three zones: In the first zone ($0<x_N/R_d<\sim10$) the fan jet mixes with the TPS wake flow; a thick shear layer results. Both the Mach and the temperature profiles of the primary jet don't change significantly. The wake of the plug and the core cowl disappears. It is, however, not yet clear wether the sudden widening of the secondary jet at about x_N/R_d=8 ($\equiv x/L$=1.8) is physical or a numerical effect. Nevertheless, the effect is also shown in the pressure distributions above the TPS (figure 18). In the second zone ($\sim10<x_N/R_d<\sim30$) the shear layer of the fan jet disappears and the core of the primary jet doesn't change, only the width of the shear layer increases slightly. In the third zone ($x_N/R_d>\sim30$) the jet disperses. The profiles of all quantities become more and more even, i.e. the flow becomes more and more homogeneous.

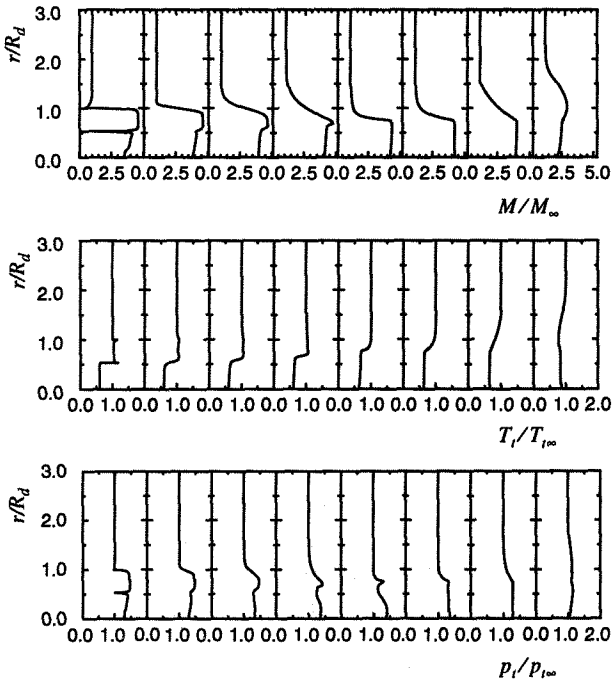

Fig. 21: Mach number, temperature and stagnation pressure profiles of the TPS jet

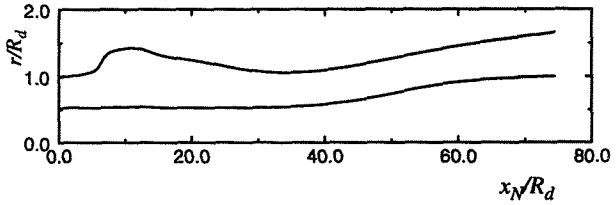

Fig. 22: Streamlines behind the TPS

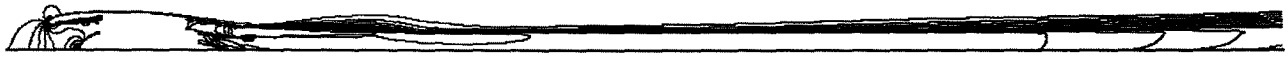

Fig. 20: Mach number isolines of the TPS

Conclusion

In this paper the results of a numerical investigation are presented. The flow fields about a turbofan engine and its wind tunnel simulator are compared. The simulation quality of the TPS technique is reduced since its jet characteristics and its effects on the surrounding flow field show significant differences to the scaled down actual engine. Since the interference of the engine and its jet with the wing can change the flight characteristic significantly it is important to match these effects of the engine as good as possible. This requirement gains an increasing importance for high bypass engines with engine integrations close to the wing.

The largest differences of a TPS and an actual engine result out of the TPS jet. It is a jet with about 0.6 *kg/s* more mass flow compared with the scaled engine. The cold primary jet with a high density is isolated by the fan jet but the mixing procedure of the TPS jet differs from the actual one. The differences of the inlet flow of the TPS and the scaled engine lead to different drag coefficients since the friction drag coefficient is similar for both engines. These effects have an local character and they don't influence the interference effects in the rear part of the engine.

Only three-dimensional axisymmetrical engine flows are calculated because of the basic character of this comparison. Nevertheless it is possible to calculate the three-dimensional unsymmetrical engine flows to obtain a more realistic picture for example of the inlet and the nozzle flow, of course, at the prise of a higher numerical expenditure.

Acknowledgement

The authors would like to thank Deutsche Aerospace Airbus GmbH, Bremen and MTU GmbH, München for the kind provision of data used in this investigation.

References

[1] Oates,G.:
Aerodynamics of Gas Turbine and Rocket Propulsion
AIAA Education Series, AIAA Inc. Washington, 1988

[2] Geidel,H.A., Eckardt,D.:
Gearless CRISP -The Logical Step to Economic Engines for High Thrust
Proceedings of the 9th ISABE, Athen 1989

[3] Rossow,C.-C.,et al.:
Investigation of Propulsion Integration Interference Effects on a Transport Aircraft Configuration
AAIA 28th Joint Propulsion Conferenc and Exhibition
Nashville, TN, July 1992

[4] Burgsmüller,W.; Castan,C.; Kooi,J.W.:
Engine Integration on Transport Aircraft -Status and Prospects-
European Forum of Wind Tunnels and Wind Tunnel Techniques. Southampton /GB 14.-17.9.92

[5] Bolms, H.-Th.:
Auslegung eines 'single-rotating' Propfan-Simulators auf ADP-Basis für den Windkanalversuch
DLR-IB 29112 - 91A08, DLR Göttingen, 1991

[6] Schwamborn, D. :
Simulation of the DFVLR-F5 Wing Experiment using a block structured explicit Navier-Stokes Method
Notes on Numerical Fluid Mechanics, Volume 22
Vieweg, Braunschweig 1988

[7] Baldwin, B.; Lomax, H. :
Thin-Layer Approximation and Algebraic Model for Seperated Turbulent Flow
AIAA-78-257, 1978

[8] Granville, P. S. :
Baldwin-Lomax Factors for Turbulent Boundary Layers in Pressure Gradients
AIAA Journal, Vol. 25, No. 12, Technical Notes, 1987

[9] Wilcox, D. C. :
Reassesment of the Scale-Determining Equation for Advanced Turbulence Models
AIAA Journal, Vol. 26, November 1988

[10] Jameson, A. ; Schmidt, W. ; Turkel, E. :
Numerical Solutions of the Euler Equations by Finite Volume Methods Using Runge-Kutta Time-Stepping Schemes
AIAA-81-1259, 1981

[11] Ronzheimer, A., et al.:
A New Interactive Tool for the Management of Grid Generation Process around Arbitrary Configurations
4th International Conference on Numerical Grid Generation in Computational Fluid Dynamics and Related Fields, Swansea UK, April 1994

[12] Rossow,C.-C.:
Berechnung von Strömungsfeldern durch Lösung der Euler-Gleichungen mit einer erweiterten Finite-Volumen Diskretisierungsmethode
DLR-FB 89-38, DLR Braunschweig, 1989

[13] Mason,M.L.; Putnam,L.E.:
Pitot Pressure Measurements in Flow Fields behind Circular-Arc Nozzles with Exhaust Jets at Subsonic Free-Stream Mach Numbers
NASA TM 80169, 1979